CFD modeling of flow and local scour around submerged bridge decks

Gábor Fleit[1,2,3], Sándor Baranya [1,3], Ronja Ehlers [4], Hans Bihs [4]

Abstract

The level set method-based, multiphase hydro- and morphodynamic numerical model REEF3D is used for the simulation of the flow conditions and local scouring around submerged bridge decks. Presence of hydraulic jumps, bridge overtopping, pressurized jets and the resulting scouring make the selected test cases especially challenging from the numerical modelling point of view. The models are validated against experimental data. The influence of the submergence ratio on the prevailing flow and scouring is investigated. The level set method showed robustness and good accuracy for the treatment of the complex free surface as well as for the tracking of the mobile bed. The submergence ratio showed no clear correlation with the prevailing erosion/deposition patterns. As the simulations offered insights into the prevailing hydrodynamics and thus the relevance of numerical modelling was emphasized for such complex sediment transport problems.

Keywords

CFD modeling, free surface flow, pressure scour, RANS model, sediment transport, submerged bridge

[1] fleit.gabor@emk.bme.hu, baranya.sandor@emk.bme.hu, Department of Hydraulic and Water Resources Engineering, Faculty of Civil Engineering, Budapest University of Technology and Economics, Budapest, Hungary
[2] HUN-REN-BME Water Management Research Group, Hungarian Research Network, Budapest, Hungary
[3] National Laboratory for Water Science and Water Safety, Budapest University of Technology and Economics, Budapest, Hungary
[4] ronja.ehlers@ntnu.no, hans.bihs@ntnu.no, Department of Civil and Environmental Engineering, Norwegian University of Science and Technology.

1 Introduction

Extreme hydrological events like flash floods occur ever more frequently as a result of the global climate change (Kundzewicz et al., 2013). Higher discharges mean increased flood risk through higher water levels. The consequently higher flow velocities entail increased stresses on the riverbeds and on hydraulic engineering structures. The increased stress can indirectly (or in extreme cases even directly) endanger the stability of bridges, providing an eternal design and research challenge for the civil engineering society. One of the major reasons of bridge failures are scour hole formations around their support structures (Johnson and Ayyub, 1992). Scour holes tend to continuously develop over time during ordinary flow conditions; however, flood events often have major impacts on the bed morphology, especially in the proximity of such structures (Deng and Chai, 2010).

Smaller bridges are often designed to withstand 100-year flood events due to reasonable economic considerations. The related smaller rivers (with smaller catchments) are usually more exposed to short period extreme (flash) floods than rivers of larger catchments. During such events, the water level may even reach the bridge deck, resulting in intense mechanical, hydrodynamic and morphodynamic responses. Considering that there are no ultimate formulas available for the quantification of local scouring in the vicinity of bridge piers, the prediction of the morphodynamic changes around fully or partially submerged bridges is even further away from being trivial. Bridges that become inundated during floods are subject to pressurized flow conditions, which not only makes the prediction of the hydraulic conditions more difficult but can create and aggravated scour situation as well. As the depth of the approaching flow increases, the bridge deck may become partly or entirely submerged with the resulting floodwater being directed both under and over the bridge deck (Umbrell et al., 1998). In this case, the bridge deck behaves like a broad-crested weir, while the vertical contraction caused by the bridge structure directs the flow towards the bed with increased velocities, and thus, erosion potential.

Flow and local scouring around bridge piers and abutments without overtopping have been in the focus of intense research in the past decades (e.g., Baranya et al., 2012; Kara et al., 2015a; Olsen and Melaaen, 1993; Roulund et al., 2005). Pressurized flow conditions around bridges have also been investigated since the 1990s, however, with notably fewer references in the literature. Abed (1991) investigated pressure-flow pier scours and found that at the same flow rate, 2–10 times larger scours can occur under pressurized conditions than during free surface flow. The topic was further studied by Jones et al. (1993) in laboratory conditions without bridge piers. Umbrell et al. (1998) carried on the research topic via laboratory experimentation and a theoretical approach to find out more about the nature of the relevant phenomena. A formula was proposed, explaining 81% of the variation inherent in their experimental data. The variables found to be determining the pressure flow scour depth (s_{max}) are the following: approach depth (H_0), depth and time-averaged flow velocity (U_0), total thickness of the bridge deck (D) (beams included), height of the bridge (h_b) and the critical scour velocity of the sediment forming the bed (Figure 1). A logical formulation of these variables led to Umbrell's formula. The formula has been further improved by Shen et al. (2012), based on complementary physical model experiments.
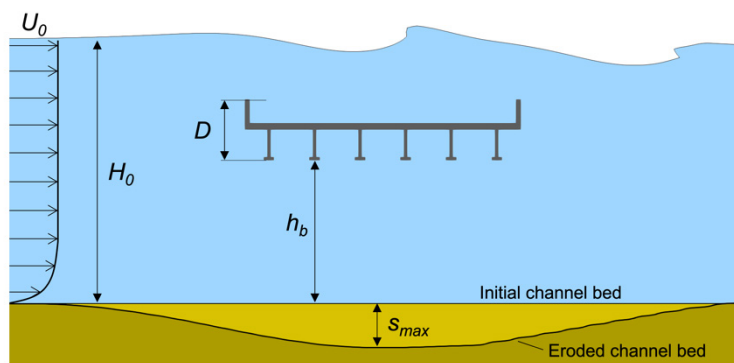

Figure 1: Schematic sketch of the studied flow problem.

The time-dependency of clear water scour under submerged bridge decks with overtopping have been investigated in laboratory conditions by Guo et al. (2009) and Guo (2011) yielding a mechanistic solution for the prediction of the scour profile and its maximal depth. It has been found that maximal scour occurs around the downstream edge of the deck. Hahn and Lyn (2010) also investigated the spatiotemporal evolution of pressure scour formation due to a vertical contraction (i.e., a partially submerged bridge deck) and reported the result that the maximal scour depth occurred at a location downstream of the contracted section. The experimental study of Kumcu (2016) focused on the differences of pressure scouring under steady and unsteady flow conditions. The temporal evolution of the scour depth and deposition height, as well as their location have been assessed. This issue of unsteady flow conditions is of key importance, as the equilibrium scour profile usually cannot develop in real conditions due to the rapid changes in the hydrograph during flood events (Guo, 2011). The low number of model variants, however, showed that the location of the maximal scour depth (even the equilibrium) can also occur on the upstream end of the contracted section. Malavasi and Guadagnini (2003, 2007) investigated hydrodynamic loads in submerged bridge decks via laboratory experiments and emphasized the importance of the prevailing free surface flow conditions on the drag forces. Martín-Vide and Prió (2006) also performed laboratory experiments to investigate the backwater effects of arch bridges and local scouring under free and submerged flow conditions.

The complex flow patterns prevailing under pressurized conditions are difficult to predict or analyze with traditional hydraulic engineering methods (i.e., laboratory experimentation). The rapid spreading of modern computational fluid dynamics (CFD) models implied the numerical investigation of hydro- and morphodynamic problems as well. The first ones to report the 3D, Reynolds-averaged Navier–Stokes (RANS) modeling of local scouring around bridge piers were Olsen and Melaaen (1993), inspiring research in the topic ever since (e.g., Roulund et al., 2005; Baranya et al., 2012, 2014). If the bridge piers or abutments are not submerged, simpler free surface treatment (Baranya et al., 2012, 2014) or even a rigid lid approach (Roulund, 2005) can be validly applied. However, in case there are submerged obstacles in the flow, the conventional (usually sigma transformation-based) methods are no longer applicable – advanced free surface treatment is required. Kara et al. (2015b) conducted the physical and computational modeling of flow over a schematic, submerged bridge geometry using a large eddy simulation (LES) solver with level set method (LSM) based free surface treatment. Their model showed good agreement with experimental data. Moreover, the LES model offered insights into the dynamic nature of the prevailing flow conditions and allowed the detection of coherent turbulent structures as well. Although examples can be found for LES-based bridge scour prediction for real life conditions (e.g., Khosronejad et al., 2020), LES in such large scales is usually computationally unaffordable.

Tulimilli et al. (2011) reported RANS-based modeling of scour under a submerged bridge deck using the commercial CFD software Star-CCM+ using a single-phase, rigid lid approach. While the shape and maximal depth of the scour whole was relatively well simulated, the measured deposition on the downstream side of the bridge deck was absent from the results. Shortcomings of Star-CCM+ and another commercial CFD model (FLOW-3D) in the simulation of local flow and local scouring around submerged bridge decks was also reported by Xie (2011).

This study aims to present the capabilities of a LSM-based CFD model for the simulation of flow and local scouring around submerged bridge decks. A Reynolds-averaged approach – considered as a computationally affordable way to solve real world problems – is used to reveal its capabilities and limitations from the hydromorphological point of view for this specific problem. Both the hydro- and the morphodynamic models are validated against experimental data from the literature. The relevance of LSM-based free surface, sediment transport and bed evolution processes is emphasized. Finally, the impact of the level of bridge deck submergence on the hydro- and morphodynamic conditions is investigated.

2   Numerical modeling

The open-source hydrodynamics framework REEF3D (Bihs et al., 2016) was used for the numerical simulations. The model has been successfully validated through a range of hydraulic engineering applications in the past, including open channel free surface flow (Fleit et al., 2018; Kamath et al., 2019) and sediment transport as well (e.g., Gautam et al., 2021; Ahmad et al., 2015; Ahmad et al., 2019; Ahmad et al., 2020).

2.1   Governing equations

The model solves the incompressible Reynolds-averaged Navier–Stokes (RANS) equations along with the continuity equation using conservative finite differences:

$$\frac{\partial u_i}{\partial x_i} = 0 \, , \qquad [1]$$

$$\frac{\partial u_i}{\partial t} + u_j \frac{\partial u_i}{\partial x_j} = -\frac{1}{\rho}\frac{\partial p}{\partial x_i} + \frac{\partial}{\partial x_j}\left((v + v_t) + \left(\frac{\partial u_i}{\partial x_j} + \frac{\partial u_j}{\partial x_i}\right)\right) + g_i \, , \qquad [2]$$

where u is the velocity averaged over time t, x is the space coordinate, ρ is the fluid density, p is the pressure, v is the kinematic viscosity, v_t is the turbulent eddy viscosity and g is the acceleration due to gravity. Indexes i and j refer to the Cartesian components of vector variables and terms containing j are implicitly summed over $i = 1\ldots3$.

The projection method (Chorin, 1968) is used for pressure treatment and the resulting Poisson's equation is solved with a geometric multigrid preconditioned BiCGStab solver (Ashby and Falgout, 1996) provided by the high-performance solver library, HYPRE (Falgout et al., 2006).

2.2 Free surface treatment

REEF3D systematically uses the level set method (LSM, Osher and Sethian (1988)) in various aspects of the modeling. In addition to the treatment of the complex free surface, LSM is used for the representation of solid boundaries (obstacle geometries) and for the simulation of the mobile bed as well. The locations of these interfaces are represented by the zero level set of a smooth signed distance function $\phi(x,t)$. The level set function gives the closest distance to the interface (Γ) and the phases are distinguished by the sign. In case of free surface (interphase between air and water phases), the level set function can be written as:

$$\phi(\boldsymbol{x},t) = \begin{cases} > 0, & if \ \boldsymbol{x} \ \epsilon \ phase \ 1 \\ = 0, & if \ \boldsymbol{x} \ \epsilon \ \Gamma \\ < 0, & if \ \boldsymbol{x} \ \epsilon \ phase \ 2 \end{cases} . \qquad [3]$$

The combined use of the LSM and the ghost cell immersed boundary method (Berthelsen and Faltinsen, 2008) allows the use of computationally efficient, static (no remeshing is required), structured, orthogonal computational grids (Bihs and Kamath, 2017).

2.3 Turbulence modeling

The effect of turbulent velocity fluctuations is represented with the eddy viscosity, following the Boussinesq-approximation. Turbulence closure is achieved with the standard k-ω model introduced by Wilcox (1994), adding additional transport equations for the turbulent kinetic energy (TKE, k) and its specific dissipation rate (ω) to the governing equations:

$$\frac{\partial k}{\partial t} + u_j \frac{\partial k}{\partial x_j} = \frac{\partial}{\partial x_j}\left(\left(\nu + \frac{\nu_t}{\sigma_k}\right)\frac{\partial k}{\partial x_j}\right) + P_k - \beta_k k\omega \,, \qquad [4]$$

and

$$\frac{\partial \omega}{\partial t} + u_j \frac{\partial \omega}{\partial x_j} = \frac{\partial}{\partial x_j}\left(\left(\nu + \frac{\nu_t}{\sigma_\omega}\right)\frac{\partial \omega}{\partial x_j}\right) + \frac{\omega}{k}\alpha P_k - \beta\omega^2 \,, \qquad [5]$$

where P_k is the turbulent production rate and the coefficients have the values $\alpha=5/9$; $\beta_k=9/100$, $\beta=3/40$, $\sigma_k=\sigma_\omega=2$. The artificial overproduction of turbulence around of the free surface (due to the high gradients in fluid properties) is overcome with free surface turbulence damping proposed by Kamath et al. (2019).

2.4 Discretization

The weighted essentially non-oscillatory (WENO) scheme (minimum 3rd-order, but up to 5th-order accurate) of Liu et al. (1994) is applied to discretize the convective terms of the RANS equations, providing high accuracy and robust numerical stability. The level set function, turbulent kinetic energy and specific turbulent dissipation rate are treated with the Hamilton-Jacobi formulation of the WENO scheme (Jiang and Peng, 2000). Time advancement in the governing equations is treated with a 3rd-order total variation diminishing Runge-Kutta scheme (Gottlieb and Shu, 1998).

Computational efficiency is achieved with adaptive time stepping based on the Courant–Friedrichs–Lewy (CFL) criterion and parallelization through domain decomposition. The neighboring parts of the computational domain communicate through ghost cells, whose data exchange is treated with the message passing interface (MPI).

2.5 Sediment transport

Bed shear stress (BSS) is calculated based on the assumption that the turbulence production and its dissipation are in equilibrium close to the bed. Hence, BSS (τ_b) is related to the turbulent kinetic energy near the bed as follows:

$$\tau_b = \sqrt{C_\mu} \rho k \,, \tag{6}$$

where $C_\mu = 0.09$ (Rodi, 1980).

Bedload transport rate (q_b) is accounted for through Shields' semi-empirical approach based on the critical bed shear stress (τ_c):

$$\tau_c = \tau_c^* (\rho_s - \rho) g d, \tag{7}$$

where τ_c^* is the non-dimensional Shields number, ρ_s is the density of the sediment and d is the characteristic sediment particle size. The critical shear stress is calculated with the longitudinal and transversal slopes of the local sediment bed being accounted for, using the explicit formulation of Dey (2013). The bed load rate is calculated with the formulation proposed by van Rijn (1984):

$$\frac{q_b}{d^{1.5} \sqrt{\frac{(\rho_s - \rho) g}{\rho}}} = 0.053 \frac{\left(\frac{\tau_b - \tau_c}{\tau_c}\right)^{2.1}}{d^{0.3} \left[\frac{(\rho_s - \rho) g}{\rho v^2}\right]^{0.1}} \,. \tag{8}$$

The topography of the mobile bed is numerically represented with and additional level set function, hence, no (computationally expensive) remeshing is required during bed level changes. The bed morphology is represented by a second level set function, and its motion is given by the sediment mass balance in each cell, described with Exner's equation (see e.g., Paola and Voller, 2004).

The sand slide algorithm (Burkow, 2016) is employed, which acts as a limiter for the bed shear stress reduction. As erosion starts in a cell, the bed locally gets tilted, which results in the reduction of the critical bed shear stress. This results in further erosion and so on. Whenever the bed slope exceeds the angle of repose of the bed material, the slope of the concerned bed cell is readjusted by redistributing the volume of sediment in the neighboring cells in an iterative manner – the iterations stop, when the local slope reaches the angle of repose). In case of 2DV modeling, this means a modification of the two neighboring bed cells by $\Delta h/6$, where Δh is the height difference between the adjacent cells. The sand slide algorithm is not only necessary for numerical stability, but also represents an actual physical process.

In order to reduce the computational demand of sediment transport simulations, a decoupled time stepping approach is used. With that, the bed load transport and the resulting bed level changes are treated with much larger time steps than the governing hydrodynamic equations. The sediment transport time steps are also adaptively controlled through the CFL criterion based on the rate (time derivative) of the bed elevation changes. Morphodynamic changes are evaluated after every fifth hydrodynamic time step so that the flow can always adapt to the prevailing bed level changes.

3 Numerical scenarios

3.1 Flow around a bridge deck with overtopping

The first case study is based on the experimental work of Chu et al. (2016). Here, the main goal is the validation of the RANS model, as well as the conduction of a grid convergence study. The original experiments were performed in a circulating, rectangular, flatbed flume of 1.10 m length and 0.12 m in width. A rectangular obstacle (schematized bridge deck) was placed in the channel with a length of $L = 0.03$ m and a thickness of $D = 0.01$ m. The distance between the channel bed and the underside of the deck was $h_b = 0.036$ m. The upstream water depth ($H_0 = 0.056$ m) was kept constant during the experiments with a controlled tailwater level. The time and depth averaged inflow flow velocity was $U_0 = 0.43$ m s^{-1}, i.e., a specific discharge of $q = 3.58$ m^2 s^{-1} was approaching the deck (Fr = 0.58; Re = 4,300). The longitudinal free surface profile was measured during the experiments with a resolution of 0.1 mm.

Considering the lateral symmetry of the flow problem, a vertical slice (2DV) modeling approach was employed, enabling fast and computationally affordable simulations. The computational domain was 0.75 m long × 0.11 m high × 1 cell wide (Figure 2) and consisted uniform hexahedron cells. A grid convergence study was performed to find an optimal

computational mesh for the simulations. Four reasonable grid resolutions (Δx) were used ranging from $\Delta x = 2.00$ mm to $\Delta x = 0.625$ mm (Table 1). The relative grid resolution (defined as $H_0/\Delta x$) was calculated and used in the grid sensitivity analysis – ultimately showing the number of cells along the approach depth necessary for the proper solution of the flow problem.

Table 1: Computational mesh parameters in the grid convergence analysis used for the hydrodynamic case study. The asterisk (*) marks the reference setup. N_{cells} is total number of computational cells used in a simulation.

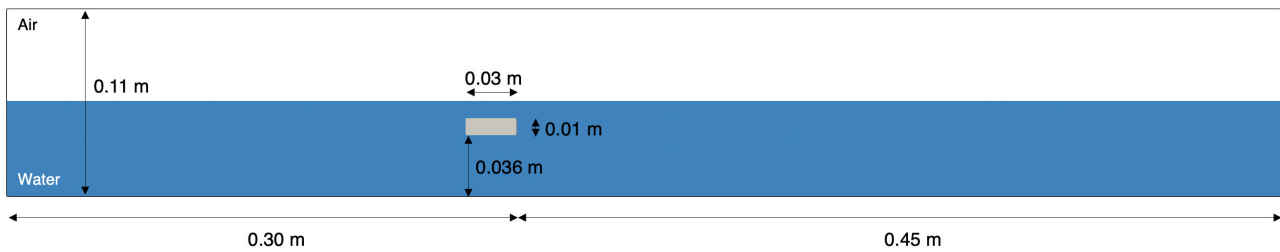| #	Δx (mm)	N_{cells} (-)	$H_0/\Delta x$ (-)
G1	2.000	20 625	28.0
G2	1.250	52 800	44.8
G3*	1.000	82 500	56.0
G4	0.625	211 200	89.6

Figure 2: Dimensions of the computational domain and the initial water level for the hydrodynamic case study. Flow direction is from left to right.

A Dirichlet-type boundary condition was defined at the inlet boundary with constant inflow water discharge. The water surface at the inlet developed freely as a part of the hydrodynamic solution. The prescribed discharge is distributed along the prevailing water column with the assumption of a logarithmic velocity profile. The sidewalls and the top of the domain were defined as symmetry planes, whereas the bottom was defined as a no-slip, wall-type boundary. The prescribed outflow water level was fixed using a zero-gradient (Neumann-type) boundary condition. The simulations were run until convergence, then the resulting free surface profiles were compared with experimental data.

3.2 Local scour under a submerged bridge deck

The second case study is based on the experimental work of Guo (2011) and focuses on the verification of the morphodynamic model. The original experiments were performed in a narrowed section of a larger flume. The test section was 3.00 m long × 0.55 m high × 0.64 m wide. A six-girder bridge deck ($L = 0.26$ m) was placed in the flume (Figure 3b). The distance between the initial sediment bed and the lowest point of the deck was $h_b = 0.135$ m. The upstream water depth ($H_0 = 0.25$ m) was kept constant during the experiments with a controlled tailwater level. The mean inflow velocity was $U_0 = 0.485$ m s^{-1}, that is, a specific discharge of $q = 0.121$ m^2 s^{-1} was approaching the obstacle (Fr = 0.31; Re = 66,700). The mobile bed consisted of well-graded ($\sigma_g = 1.35$, where $\sigma_g = D_{84}/D_{16}$ and D_{84} and D_{16} are 84 and 16 percentiles of the grain size distribution, respectively) very fine sand with a median particle diameter of $d = d_{50} = 2.18$ mm. The scour profile was measured with a laser distance sensor (accuracy of ±0.2 mm).

Similarly to the previous case, the flow problem is laterally symmetrical, allowing a 2DV approach. The assumption is also supported by Guo et al. (2009), who reported that the experimental conditions – and the evolving scour in particular – are basically two-dimensional. The computational domain was 2.50 m long × 0.6 m high × 1 cell wide (Figure 3a). The lowest 10 cm of the domain is the erodible sediment bed.
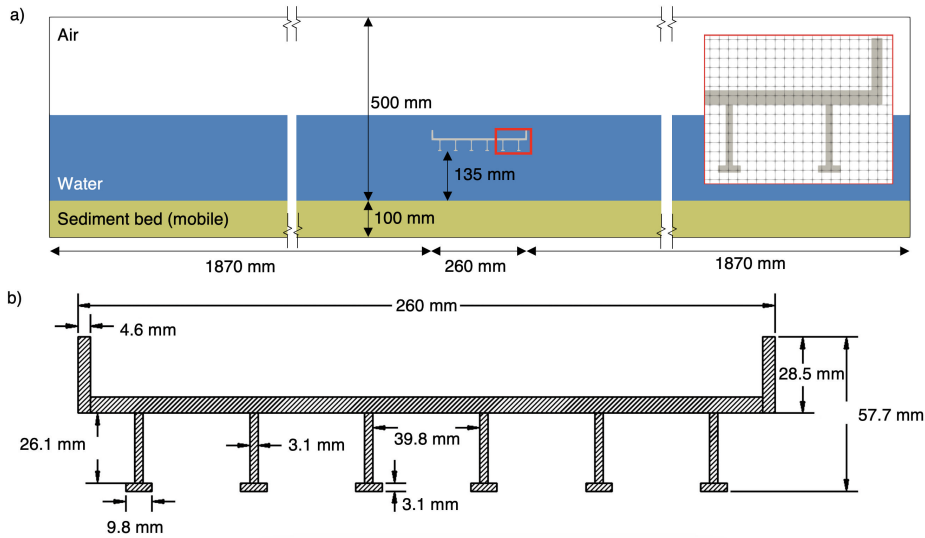
Figure 3: (a) Numerical setup for the morphodynamic case study and detail of the computational mesh near the bridge geometry in the magnified view; (b) geometry of the six-girder bridge deck. Flow direction is from left to right.

In absence of experimental hydraulic data, the hydrodynamic model could not be directly verified in this case. In order to ensure the reliability of the results, the resolution of the computational mesh was selected based on the findings of the grid convergence study of the previous case study (see later). The selected resolution was $\Delta x = 4.0$ mm, which corresponded to a relative grid resolution of $H_0/\Delta x = 62.5$.

The boundary conditions were defined in the same manner as in the previous case. First, the hydrodynamic simulation was computed until convergence, and only then was the sediment transport routine started and run for 42 hours (time required for quasi-equilibrium conditions during Guo's (2011) experiments). The steady state (rigid bed) simulations took approximately 0.5 hours, the mobile bed cases around 10 hours of CPU time (10 core Apple M1 Pro) on a personal notebook.

3.3 Influence of submergence ratio

After the verification of the hydro- and morphodynamic models, the influence of the submergence (h^*) ratio on the prevailing flow conditions and scouring is investigated via numerical experiments. The submergence ratio is defined as the ratio of water depth from the surface to the bottom of the deck and the vertical width of the deck:

$$h^* = \frac{H_0 - h_b}{D} \ .$$

[9]

The basis of the simulations was the morphodynamic case study; only the upstream water levels were altered to achieve various overtopping scenarios. The simulations were again performed in two steps: i) the hydrodynamic models were run until steady state with a fixed bed (simulations H1–H3); then ii) the results were used as initial conditions for the morphodynamic simulations (S1–S3). The most relevant parameters and some describers of the prevailing flow conditions are summarized in Table 2.

Table 2: Relevant parameters of the numerical experiments with different levels of submergence. The asterisk (*) marks the setup used for the verification of the morphodynamic model.

#	U_0 (ms^{-1})	H_0 (m)	h^* (-)	Submergence	Overtopping	Bed
H1	0.485	0.25	2.00	Full	Yes, with undular hydraulic jump	Fixed
S1*						Mobile
H2	0.485	0.21	1.30	Full	Yes, with submerged hydraulic jump	Fixed
S2						Mobile
H3	0.485	0.17	0.61	Partial	-	Fixed
S3						Mobile

4 Results

The results of numerical simulations are summarized in the following order: i) the verification of the hydrodynamic model is presented based on the experimental data of Chu et al. (2016); ii) then the morphodynamic model is validated against the data from Guo (2011); and iii) finally, the influence of the submergence ratio on the hydraulic and morphodynamic behavior is investigated.

As a first step of the hydrodynamic verification, a qualitative comparison of the measured and simulated flow condition is presented in Figure 4. It is observed that the general nature of the flow is captured by the numerical model. Considering the inherent limitations of a RANS solution, the location of the hydraulic jump is predicted accurately, whereas the marked drop of the water levels on the downstream side of the deck is smoothed out. This also entails the overprediction of the water levels above the deck itself. Such discrepancy of RANS models in cases of complex flows with significant streamline curvature and body force effects have already been reported by Lee et al. (2010).
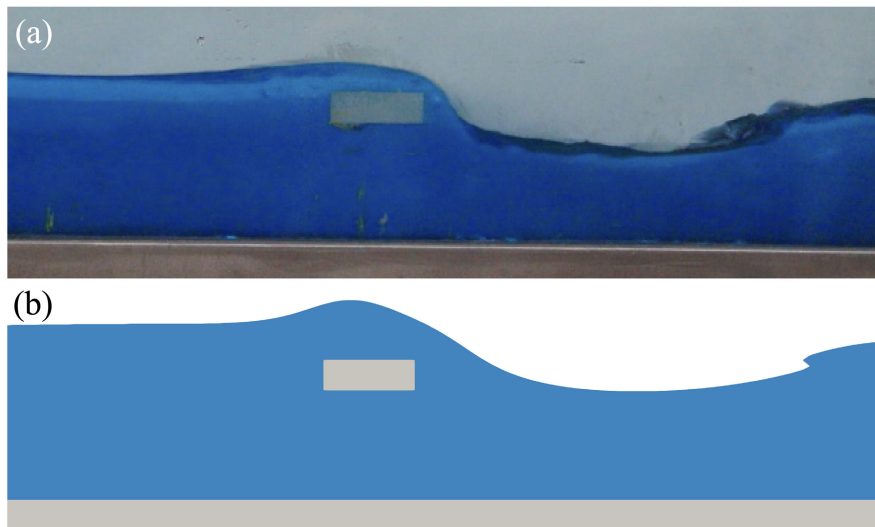

Figure 4: Qualitative comparison of the experimental conditions (a) and time-averaged numerical model (G3) result (b). Photograph source: Chu et al., 2016.

The model verification and the grid convergence study are based on the comparison of measured and modeled longitudinal free surface profiles (Figure 5a). To put the RANS results into context, LES results from the original paper (Chu et al., 2016) are also plotted. It is observed that the general features of the flow problem are present even in the lowest resolution model variant (G1). The second coarsest variant (G2) predicts the hydraulic jump to be closer to the deck. G1 shows the largest overprediction of the upstream water depth and at the location of the hydraulic jump as well. G1 and G2 performs the worst between the deck and the hydraulic jump ($x = 0.34$–0.39 m). It is noted that the water levels in this section are also overestimated by the LES results of Chu et al. (2016). Although the high surface gradient in the vicinity of the deck is captured notably better by LES, the finer resolution RANS solutions (G3, G4) offer slightly better results on the upstream end of the hydraulic jump ($x = 0.35$–0.40 m). The location of the hydraulic jump and the corresponding water levels are also reproduced well with both G3 and G4.
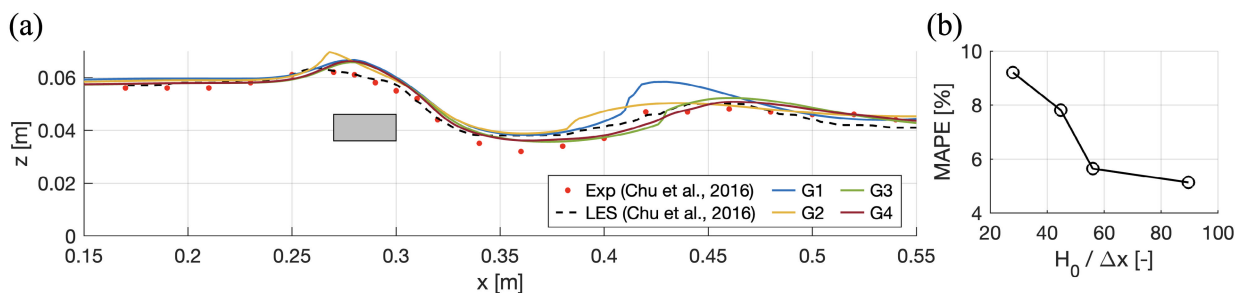

Figure 5: Verification of the hydrodynamic model (a) and the results of the grid convergence study (b).

The accuracy of the four variants was quantified through the mean absolute percentage error, $MAPE = \frac{100\%}{n}\sum_{i=1}^{n}\left|\frac{m_i-s_i}{m_i}\right|$ (where m_i and s_i denote measured and simulated water level values at n points, respectively). The results are interpreted through the relative (dimensionless) grid resolution, $H_0/\Delta x$ (Figure 5b). The accuracy rapidly improves between $H_0/\Delta x = 28–56$ (G1–G3), then the convergence slows down between the two higher resolution variants (G3, G4). Based on the comparison of the free surface profiles and the grid convergence, it is assumed that a relative cell size of $H_0/\Delta x = 60$ (that is, 60 computational cells along the upstream depth) is sufficient for the solution of the flow problem around a submerged bridge deck.

Considering the model verified, the prevailing flow conditions for the reference setup (G3) are assessed based on the simulation results (Figure 6). The submerged jet and the consequent increase of near-bed TKE implies the potential for local erosion and the development of a pressure scour. The highest flow velocities and near-bed TKE values are observed below the section with the depressed water levels upstream the hydraulic jump. The separation around the deck entails locally increased velocities up to 0.80 m s^{-1}, and the highest TKE is observed in this area as well.
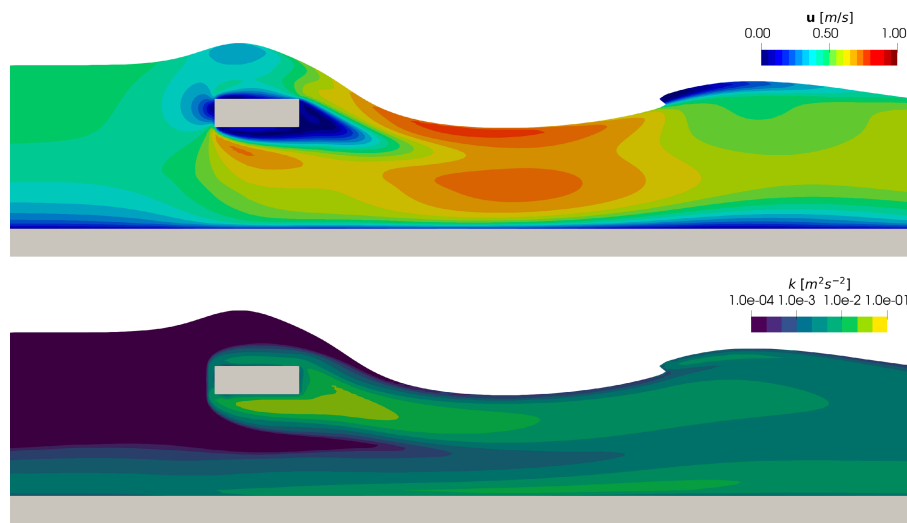

Figure 6: Modeled distribution of time-averaged velocity magnitude (top); and the turbulent kinetic energy (bottom) with a logarithmic colormap. Only the relevant section of the computational domain is shown.

After the verification of the hydrodynamic model, the focus is moved towards local scouring. The experimental data of Guo (2011) is used to validate the morphodynamic model. In absence of hydrodynamic control data for these experiments, the assumption is made regarding the sufficient grid resolution based on the findings of the previous case study (considering the general geometrical similarities between the two cases). A relative grid resolution of $H_0/\Delta x = 62.5$ ($\Delta x = 2.0$ mm) is used for morphodynamic modeling cases.

The prevailing flow conditions prior to the initiation of sediment transport and after reaching the equilibrium scour are presented in Figure 7. In comparison with the previous case study, a more intense submerged jet is observed below the deck. The higher tailwater level also alters the general nature of the flow: a standing wave formation is observed in both cases. During the scouring process, the flow slowly rearranges, allowing for the attenuation of the flow velocities both below and above the deck. Although velocities notably decrease, the general features of the flow are preserved – the submerged jet, as well as the standing wave formation is observed in case of the equilibrium scour as well.
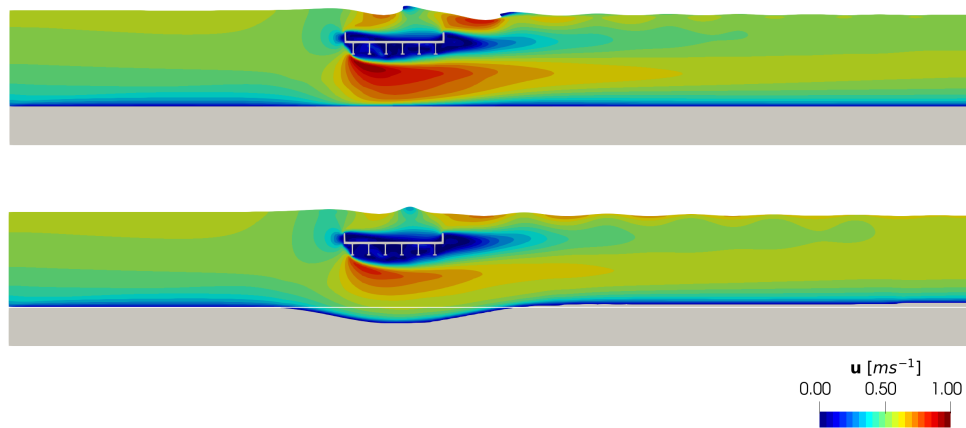
Figure 7: Velocity magnitude distribution before (top) and after 42 hours of sediment transport time (bottom).

The comparison of the measured and simulated equilibrium scour profiles shows reasonable agreement (Figure 8a). The general shape of the scour profile and the (x-wise) start of the erosion and deposition sections are accurately reproduced by the numerical model. The location of the maximal scour depth (and most of the scour hole itself) is slightly shifted in the upstream direction. Although the maximal deposition height is underestimated, the general nature of the morphodynamic problem is adequately captured.

The overall shape of the calculated scour profile suggests that model can resolve the underlying flow and sediment transport processes. However, notable deviations are observed in the temporal development of the maximal scour depth (s_{max}). While the predicted equilibrium scour depth is captured accurately, the numerical scouring process itself is more intense. Contrary to the observed experimental morphological equilibrium at ~36–42 hours (Guo, 2011), the maximal depth in the simulation is reached after approximately five hours (Figure 8b).
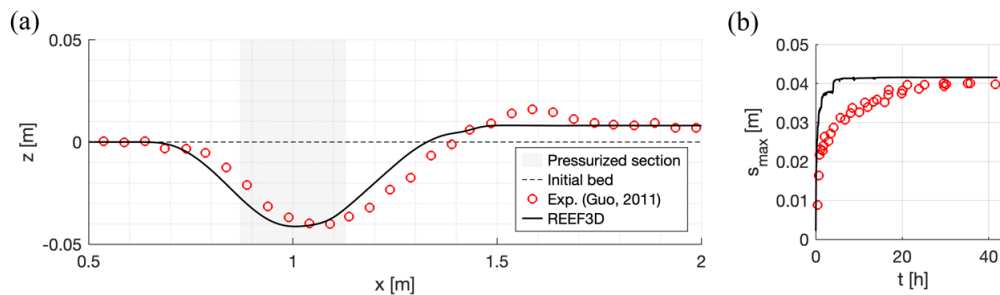

Figure 8: a) Comparison of measured and modeled equilibrium scour profiles; b) temporal evolution of maximal scour depth.

The effects of the submergence ratio on the velocity distributions before (H1–H3) and after (S1–S3) the morphodynamic simulations are investigated in Figure 9. The general flow patterns are rather similar for all cases; the different levels of submergence mostly affect the overtopping flow. In Figure 9, H1 and S1 ($h^* = 2.00$) denote the morphodynamic verification case, where the prevailing flow conditions have already been discussed. In case of $h^*=1.30$, a notable reduced water level is observed above the structure – a local standing wave formation is observed. The end of the deck acts as a weir, from which the flow plunges into the main flow forming a submerged hydraulic jump. The jet below the structure shows very similar pattern compared to the H1 variant. Downstream the deck, the surface flow after the hydraulic jump is notably slower, whereas the jet can be characterized with higher velocities in a longer distance. After the equilibrium scour profile is reached, the flow above and in the direct vicinity of the deck is basically becomes a dead zone with a less intense hydraulic jump. As a result, higher amount of water is flowing in the pressurized zone. Although the velocity distributions below the deck show very similar nature as in case of S1, this change in the distribution of discharges leads to a longer stretched scour hole (see later in Figure 12). In case of the lowest upstream water levels (H3, S3), no overtopping occurs; the flow below the deck, however, remains pressurized. The developing jet in the contraction is the mildest in this case, suggesting a more moderate scouring, which is indeed observed.
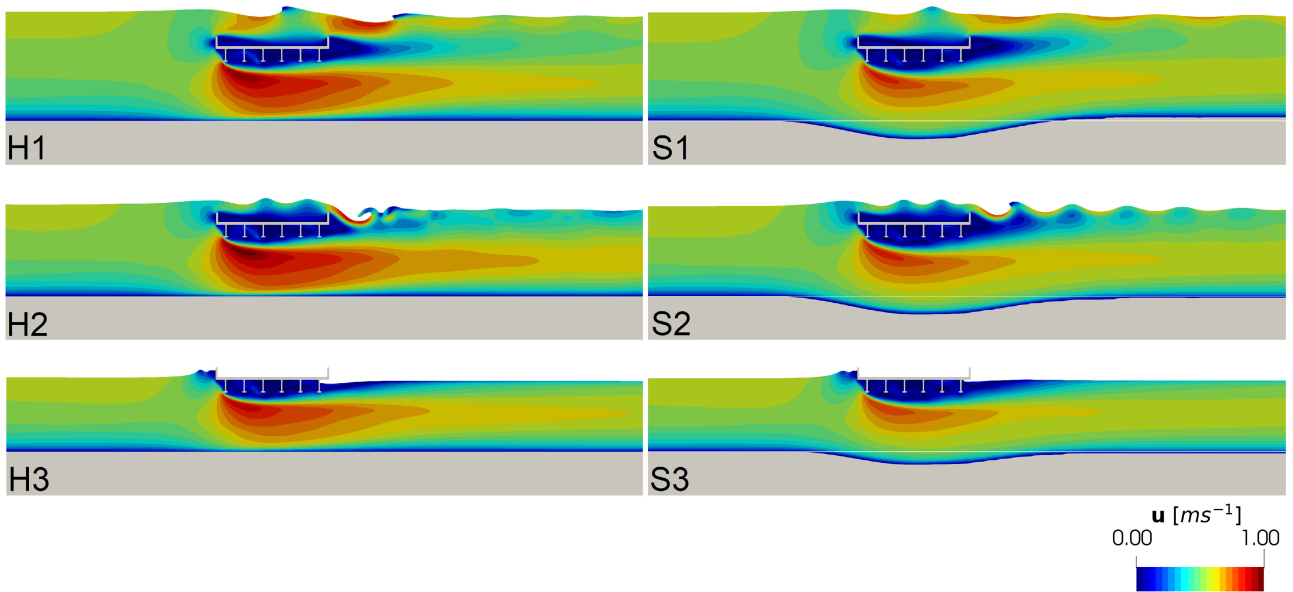
Figure 9: Velocity magnitude distributions before (H1–H3, left column) and after 42 hours of sediment transport time (S1–S3, right column) in case of different levels of submergence. Results are only shown for a section of the computational domain.

Even though the equilibrium scour depths (0.03–0.04 m) are relatively high in size compared the upstream water depths (H_0 = 0.17–0.25 m) and even more to the opening below the deck (h_b = 0.135 m) the general nature of the flow and the type of overtopping does not change as a result of the scouring process. It is also worth mentioning, that despite the initial submergence ratio, the resulting velocity distributions with the equilibrium scour show a very similar nature below the deck.

Considering the high spatial gradients in the velocity fields (Figure 9), intense turbulent conditions are expected. The spatial distributions of the TKE for the six simulation variants are presented in Figure 10. TKE, in addition to being key when interpreting RANS results through encapsulating the nature of turbulent fluctuations, also determines the sediment erosion potential of the flow (i.e., bed shear stress) through a linear relationship (Eq. 6). Notable variations are observed between the TKE fields for the fix bed simulations in the upper half water layers. As expected, the highest values occur in the direct vicinity of the deck, due to the prevailing high shears. The different types of overtopping (or the lack of it) result in different features in the vicinity of the deck. In case of H1/S1, high values develop both below and above the structure, eventually merging downstream the bridge, resulting in a massive, high TKE zone ($k > 10^{-2}$ m² s⁻²). Despite the developing hydraulic jump in H2/S2, the downstream TKE jet mostly originates from the shear below the deck. The lowest values are observed in case of H3/S3. Thus, the lowest submergence ratio results in more moderate shears.
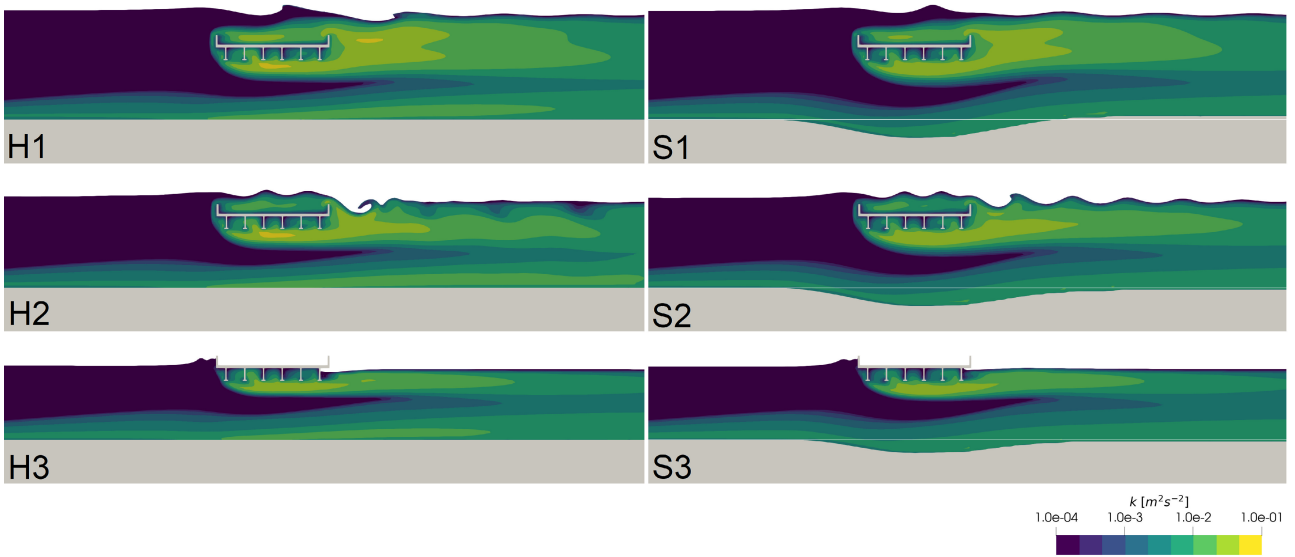
Figure 10: Turbulent kinetic energy distributions before (H1–H3, left column) and after 42 hours of sediment transport time (S1–S3, right column) in case of different submergence ratios. Note the logarithmic colormap. Results are only shown for a section of the computational domain.

On the hand, in terms of near-bed TKE, very similar patterns are observed for the fixed bed variants (H1–H3), with marked maximum values below the structure. The extension of this high TKE zone ($k > 10^{-2}$ m^2 s^{-2}) although varies between the different variants. The longest TKE jet is observed in case of H2, whereas the mildest values occur in the case without overtopping (H3). It is also worth mentioning, that the core of this high intensity, near-bed TKE jet separates from the bottom downstream the deck. High near-bed turbulent intensities coming from the upstream side of the deck (due to wall shear) merge with the obstacle-related high TKE zones of the upper layers resulting in a relatively uniform TKE distribution shortly after the structure in all cases.

As a result of scouring below the bridge, TKE distributions are locally rearranged (S1–S3). The overall patterns in the upper layers of the flow, however, basically persist. In terms of the near-bed area on the other hand, notable decrease is observed, which results in an eventual quasi-equilibrium scour profile due to the connection between TKE and bedload rate (Eqs. 6 and 7). The formerly mentioned detached TKE jet eventually disappears. The longitudinal variations of BSS are presented in Figure 11, to give a detailed look on the changes in erosion potential as a result of scour development. Results show the long-stretched effect of the near-bed TKE jet on the BSS values prior the sediment transport routine (H1–H3). The initial profiles show similar shape, with highest values reaching up to 5 N m^{-2} for the cases with overtopping and 4 N m^{-2} for H3. Peak values are observed on the downstream half of the bridge. It is noted that BSS values are above the critical threshold of the bed material both upstream and downstream of the deck. After the morphodynamic simulations, the flow is rearranged with BSS values below the critical threshold (S1–S3). Despite the different submergence ratios and the differences between the initial τ_b values, the equilibrium BSS profiles show very different shape.
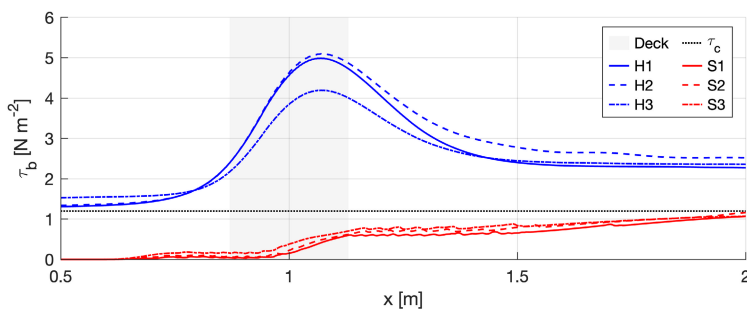

Figure 11: Longitudinal variations of final bed shear stress before (H1–H3, with blue) and after the morphodynamic simulations (S1–S3, with red). The critical shear stress is marked with the black dotted line.

The temporal evolution of maximal scour depths and the final profile of the scour hole for the three model variants (S1–S3) are presented in Figure 12. On one hand, the profiles show similar nature in terms of general shape. On the other hand, notable differences are observed in the maximal scour depths and deposition patterns (Figure 12a). In case of S1 (setup used for model verification) the already presented (Figure 8) maximal scour depth of 4.1 cm is observed with comparable sediment deposition downstream the erosion (0.9 cm). Regarding maximal scour depths, a notably lower value (3.0 cm) is observed for the case without overtopping (S3), whereas the deepest scour hole develops in case of the middle submergence ratio (S2). In contrast with S1, no sediment deposition, but a longer-lasting bottom erosion is observed in case of S2 and S3.

In terms of temporal evolution, the patterns are very similar in all cases. In all cases a short plateau is observed in the time series around $t = 1$–2 hours, where the rate of erosion is temporarily lower. This period is the shortest in case of S2 ($\sim$ 1,5 hours) and the longest in case of S1 ($\sim$ 2,5 hours). Following this section, the scour holes reach their maximum relatively fast (5 hours); then only slight changes are observed.
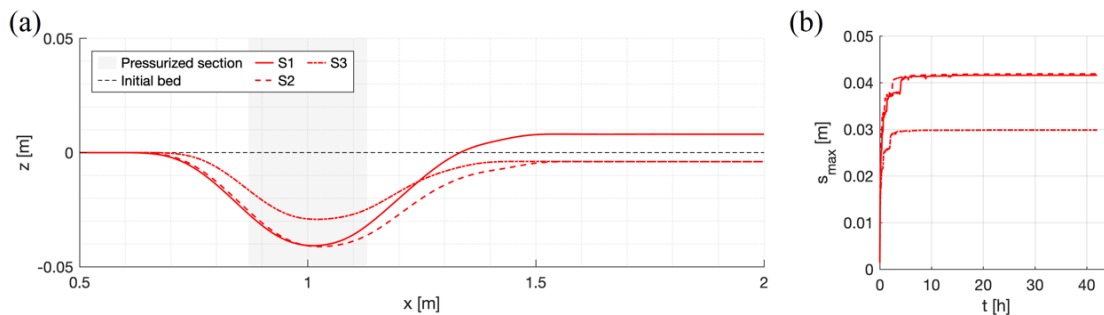

Figure 12: Equilibrium scour profiles (a) and temporal evolution of maximal scour depths (b) in cases of different levels of submergence.

Based on the model results, no tendentious connection is revealed between the submergence ratio and the maximal scour depths. A local sediment deposition is only observed in case of S1, while the deepest scouring occurs in case of S2. In terms of temporality, a very similar behavior was observed in all cases, with maximal scour depths developing after 5 hours.

5 Discussion

The potential in CFD modeling for the understanding and solution of complex – flow and sediment transport related – hydraulic engineering problems has been rapidly increasing in the past decades (Nguyen, 2004). The recent developments of such tools have encouraged researchers to investigate more and more complex flow problems and phenomena via computational modeling. State of the art CFD models can provide insights into hydro- and morphodynamic features which were formerly only assessable via costly and time-consuming experimental (laboratory) analyses at most. Nevertheless, physical modeling also has a number of shortcomings, such as scale effects (Heller, 2011) or the inherent limitations of experimental equipment.

In this study a LSM-based numerical model (REEF3D) was used to investigate the hydrodynamic conditions, as well as local scouring under submerged bridge decks. The hydro- and morphodynamic models were independently validated against experimental data from the literature (Chu et al., 2016; Guo 2011). Reynolds-averaged turbulence modeling was employed and found to be suitable for the treatment of the prevailing flow and scouring problems. The verified model was then used to analyze the hydro- and morphodynamic responses in cases of various levels of submergence. No systematic scheme was observed between the submergence ratio and the corresponding scouring. The authors note that the influence of other variables (e.g., sediment composition, bed slope, flow rate) would also worth detailed investigations in the future. The numerical results presented in this paper highlighted the different hydro- and morphodynamic behavior of a submerged bridge decks with varying approach water depths and the relevance of CFD modeling in such analyses in general.

In terms of bridges, the most frequently studied structural elements within the hydraulic engineering community are the piers. The hydrodynamic conditions (flow, turbulence, coherent structures, etc.) were subject of intensive research in

the past decades, both experimentally and numerically (see e.g., Baranya et al., 2012, 2014; Khosronejad et al., 2012; Roulund et al., 2005). Due to the lack of overtopping, the pier problem is much simpler from the aspect of free surface treatment – sigma-grid-based or other simpler single-phase approaches are usually reasonably applicable (Barany et al., 2012). In case of low Froude numbers (Fr < 0.2) even a rigid lid approach can be validly used. It is noted, that in cases of extreme flow and/or geometrical conditions, even supercritical conditions and hydraulic jumps can develop around piers (e.g., Kamath et al., 2019; Szydłowsk, 2011) which calls for advanced free surface treatment capable of capturing multiple free surface locations along a vertical (e.g., level set method or volume of fluids (Hirt and Nichols, 1981)). The problem of submerged decks, overtopping and the prevailing complex conditions, however, require advanced free surface tracking methods – hence the level set method-based model used in this study. The LSM method was found to be robust and accurate for tracking both the position of the free surface and the mobile bed as well.

Research on submerged bridge deck scouring has a relatively long history, dating back to 1990s (Abed, 1991; Jones et al., 1993; Umbrell et al., 1998), however, the topic is not considered fully resolved yet. Even the more recent studies usually exploit laboratory experiments (Guo et al., 2009, 2011; Hahn and Lyn, 2010; Martín-Vide and Prió, 2005) to understand and describe the prevailing morphodynamics. Experimental hydraulics are still often used to derive equations for the prediction of various hydraulic phenomena (in this case scour depth or even its temporal development (e.g., Guo et al., 2009, 2011)). On the other hand, physical modeling – considering its formerly mentioned limitations – usually cannot offer deep and extensive insights into the prevailing hydrodynamics. Although modern CFD modeling offers the detailed analysis of the prevailing hydromorphological conditions, such tools have barely been exploited for submerged bridges. Tulimilli et al. (2011) already presented the CFD modeling of flow and local scouring beneath a submerged bridge deck with an indirectly coupled morphodynamic model and a rigid-lid approach. Despite the notable simplifications made, the results showed the relevance of CFD modeling.

The results presented in this paper aimed to achieve progress in the CFD-based analysis of submerged bridges, offering high resolution hydrodynamics, state-of-the-art free surface tracking and directly coupled morphodynamics. Although the equilibrium scour profile was reasonably reproduced during the verification of the morphodynamic module, the model struggles to reproduce the temporal development of the scour. This is not an unprecedented behavior – many examples can be found in the literature, where equilibrium scour profiles are accurately simulated while predicting faster (Roulund et al., 2005) or slower (Khosronejad et al., 2012) development considering the whole scouring process. In general, and in the case of piers it was found that the initial phase of the scouring is well reproduced by Reynolds-averaged numerical models, as the main driver in this intense period is the locally increased bed shear stress (Khosronejad et al., 2012; Roulund, 2005). In the later phases, coherent turbulent structures (unresolved in RANS models) are responsible for the sediment transport (Daraghi, 1990; Hager, 2007). Kim et al. (2014) showed that LES is indeed capable to resolve the temporal evolution of the scour more accurately. Although the herein studied flow problem is notably different, the fact that the initial phase of the scour development was well reproduced, the following discrepancies in the temporal evolution might also be explained by the unresolved coherent structures. Considering that the location of the maximal pressure scour depth also changes over time (with a close to logarithmic relationship as per Hahn and Lyn, 2010), the time inaccuracy of the presented RANS model could be a potential cause of the phase spatial phase shift of the predicted scour profile.

A standard k-ω turbulence closure was applied with free surface turbulence dampening (Kamath et al., 2019). Despite the sprawling developments in turbulence modeling, k-ω is still considered as a reasonable, computationally economic choice and is often employed in practical engineering applications. The inherent limitation of such a RANS approach was pointed out in the hydrodynamic case study. Lee et al. (2010) also reported that a two-equation RANS model may struggle to reproduce complex flows with significant streamline curvature and body force effects. Comparing the results with experimental data and the simulation results of Chu et al. (2016), the superiority of the more advanced LES was not unanimous. While LES performed better directly above the obstacle, the herein used RANS approach gave better predictions at the surface depression on the downstream side. Nevertheless, as large eddies and coherent structures are not resolved directly, their contribution to the temporal development of the scour hole is also neglected with this approach (see Khosronejad et al., 2012 vs. Kim et al., 2014).

Although the proper solution of the hydrodynamic conditions is of key importance in morphodynamic simulations, the uncertainties around the available bedload transport formulas should always be considered as well. There are several widely used semi-empirical formulas available (Meyer-Peter and Müller, Einstein, Engelund and Fredsøe, Parker, van Rijn, etc.), meaning that for a specific problem, even the selection of a formula can also be considered as a way of

calibration. Moreover, the mere numerical implementation of a sediment transport model and the related routines (e.g., critical shear stress reduction, sand-slide algorithm) also make way for additional calibration and tuning. The critical Shields parameter (providing a distinct threshold for the initiation of the bedload) also plays a crucial role and its chosen value also ranges widely in the literature (0.03–0.06). In the light of the above, it can be suspected that a morphodynamic simulation with a perfect fit is also a result of the proper combination of the related routines, formulas and variables.

The general phenomenon of flow and local scouring within such pressurized conditions is, not new for the hydraulic and coastal engineering society. The popular topic of pipeline scouring is rather similar from the practical point of view (Ahmad et al., 2019; Liang et al., 2005), however, these cases usually not involve a complex free surface. The investigated cases in this study were all assuming an obstacle of infinite width, hence the 2DV modeling approach. Nonetheless, Liang et al. (2022) have recently pointed out the notable influence of the obstacle width (i.e., size in the third dimension) on the scouring through a 3D numerical pipeline scour case study. A fully 3D approach is also inevitable when coherent turbulent structures are to be resolved in the simulations.

6   Conclusions

A level set method-based CFD model (REEF3D) was used to simulate the complex hydro- and morphodynamic processes around submerged bridge decks. Simulation results were compared with experimental data through two case studies from the literature – the hydrodynamic and sediment transport module of the used CFD model was independently verified.

Simulations offered insights into the prevailing hydrodynamics in different approach depth scenarios and showed the relevance of modern CFD modeling within such complex conditions (complex free surface patterns, hydraulic jumps, pressurized flow). Results showed no unequivocal relationships between the submergence ratio and the resulting erosion process, suggesting that the scouring is highly case specific and depends on local features of the prevailing flow conditions.

Relevant shortcomings and possible ways of improvements were discussed in the light of the results and recent examples from the literature. The employed 2DV approach and the RANS turbulence modeling provided computationally efficient simulations with reasonable accuracy for the solution of practical engineering problems. A fully 3D LES approach could further improve accuracy (and our general understanding of the relevant phenomena) at the cost of orders of magnitudes higher computational times.

Acknowledgements

Author contributions (CRediT)

GF: conceptualization, numerical simulations, validation, visualization, writing – original draft; SB: conceptualization, supervision, writing – review and editing; RE: conceptualization, model testing; HB: conceptualization, software, methodology, supervision, writing – review and editing.

Nomenclature

d = characteristic sediment particle size (m)

d_{50} = median particle diameter (m)

D = thickness of the bridge deck (m)

Fr = Froude number (-)

g = gravity acceleration (m s^{-2})

h_b = height of the bridge (m)

h^* = submergence ratio (m)

H_0 = approach flow depth (m)

k = turbulent kinetic energy (m^2 s^{-2})

L = length of the bridge deck

m_i = measured value of a variable

N_{cells} = total number of computational cells (-)

p = pressure (Pa)

P_k = turbulent production rate (m^2 s^{-3})

q = specific discharge (m^2 s^{-1})

q_b = bedload transport rate (m^3 s^{-1})

Re = Reynolds number (-)

s_i = simulated value of a variable

s_{max} = simulated value of a variable

t = time (s)

u = time-averaged flow velocity (m s^{-1})

U_0 = approach flow velocity (m s^{-1})

x = Cartesian coordinate (m)

Δh = height difference between adjacent bed cells (m)

Δx = computational grid resolution (m)

ϕ = level set function (-)

ρ = volumetric density of water (kg m^{-3})

ρ_s = volumetric density of sediment particles (kg m^{-3})

σ_g = sediment gradation coefficient (-)

v = kinematic viscosity (m^2 s^{-1})

v_t = turbulent eddy viscosity (m^2 s^{-1})

τ_b = bed shear stress (Pa)

τ_c = critical bed shear stress of sediment particle (Pa)

τ_c^* = Shields parameter (-)

ω = specific turbulent dissipation rate (s^{-1})

References

Ahmad, N., Bihs, H., Kamath, A. and Arntsen, Ø.A. (2015) Three-dimensional CFD modeling of wave scour around side-by-side and triangular arrangement of piles with REEF3D. Procedia Engineering, 116:683–690. DOI:10.1016/j.proeng.2015.08.355.

Ahmad, N., Bihs, H., Myrhaug, D., Kamath, A. and Arntsen, Ø.A. (2019) Numerical Modelling of Pipeline Scour under the Combined Action of Waves and Current with Free Surface Capturing, Coastal Engineering, Vol. 148, pp. 19-35, DOI: 10.1016/j.coastaleng.2019.02.008.

Ahmad, N., Kamath, A. and Bihs, H. (2020) 3D Numerical Modelling of Scour around a Jacket Structure with Dynamic Free Surface Capturing, Ocean Engineering, Vol. 200, DOI: 10.1016/j.oceaneng.2020.107104.

Ashby, S. F. and Falgout, R. D. (1996) A parallel multigrid preconditioned conjugate gradient algorithm for groundwater flow simulations. Nuclear Science and Engineering, 124(1):145–159. DOI:10.13182/NSE96-A24230.

Baranya, S., Olsen, N.R.B., Stoesser, T. and Sturm, T.W. (2012) Three-dimensional RANS modeling of flow around circular piers using nested grids. Engineering Applications of Computational Fluid Mechanics 6(4):648–662. DOI:10.1080/19942060.2012.11015449.

Baranya, S., Olsen, N. R. B., Stoesser, T. and Sturm, T.W. (2014) A nested grid based computational fluid dynamics model to predict bridge pier scour. Proceedings of the Institution of Civil Engineers: Water Management, 167(5):259–268. DOI:10.1680/wama.12.00104.

Berthelsen, P. A. and Faltinsen, O. M. (2008) A local directional ghost cell approach for incompressible viscous flow problems with irregular boundaries. Journal of Computational Physics, 227(9):4354–4397. DOI:10.1016/j.jcp.2007.12.022.

Bihs, H. and Kamath, A. (2017) A combined level set/ghost cell immersed boundary representation for floating body simulations. International Journal for Numerical Methods in Fluids, 83(12):905–916. DOI:10.1002/fld.4333.

Bihs, Hans, Kamath, A., Alagan Chella, M., Aggarwal, A. and Arntsen, Ø. A. (2016) A new level set numerical wave tank with improved density interpolation for complex wave hydrodynamics. Computers and Fluids, 140:191–208. DOI:10.1016/j.compfluid.2016.09.012.

Burkow, M. and Griebel, M. (2016) A full three dimensional numerical simulation of the sediment transport and the scouring at a rectangular obstacle. Computers and Fluids, 125:1–10. DOI:10.1016/j.compfluid.2015.10.014.

Chorin, A.J. (1968) Numerical solution of the Navier – Stokes equations. Mathematics of Computation 22(104):745–762. DOI:10.1090/S0025-5718-1968-0242392-2.

Chu, C-R., Chung, C-H., Wu, T-R., Want, Y-C. (2016) Numerical analysis of free surface flow over a submerged rectangular bridge deck. Journal of Hydraulic Engineering 142(12):04016060, 11p. DOI:10.1061/(ASCE)HY.1943-7900.0001177.

Dargahi, B. (1990) Controlling Mechanism of Local Scouring. Journal of Hydraulic Engineering 116:1197–1214. DOI:10.1061/(ASCE)0733-9429(1990)116:10(1197).

Deng, L. and Cai, C. S. (2010) Bridge Scour: Prediction, Modeling, Monitoring, and Countermeasures—Review. Practice Periodical on Structural Design and Construction, 15(2):125–134. DOI:10.1061/(asce)sc.1943-5576.0000041.

Dey, S. (2001) Experimental studies on incipient motion of sediment particles on generalized sloping fluvial beds. Journal of Sediment Research, 16(3):391–398.

Falgout, R. D., Jones, J. E. and Yang, U. M. (2006) The design and implementation of hypre, a library of parallel high performance preconditioners. Lecture Notes in Computational Science and Engineering, 51:267–294. DOI:10.1007/3-540-31619-1_8.

Fleit, G., Baranya, S. and Bihs, H. (2018) CFD modeling of varied flow conditions over an ogee-weir. Periodica Polytechnica Civil Engineering, 62(1):26–32. DOI:10.3311/PPci.10821.

Fleit, G., Baranya, S., Bihs, H. (2022) CFD modeling of flow and local scouring in the vicinity of submerged bridges. In Proceedeings of the 39th IAHR World Congress, 19–24 June 2022, Granada, Spain. DOI:10.3850/IAHR-39WC2521716X2022851.

Gottlieb, S. and Shu, C.-W. (1998) Total variation diminishing Runge-Kutta schemes. Mathematics of Computation, 67(221):73–85. DOI:10.1090/s0025-5718-98-00913-2.

Gautam S., Dutta D., Bihs H., Afzal M.S. (2021) Three-dimensional Computational Fluid Dynamics modelling of scour around a single pile due to combined action of the waves and current using Level-Set method, Coastal Engineering, Vol. 170, Nr. 104002, DOI: 10.1016/j.coastaleng.2021.104002.

Guo, J. (2011) Time-dependent clear-water scour for submerged bridge flows. Journal of Hydraulic Research, 49(6):744–749. DOI:10.1080/00221686.2011.616364.

Guo, J., Kerenyi, K., Pagan-Ortiz, J. E. and Flora, K. (2009) Bridge pressure flow scour at clear water threshold condition. Transactions of Tianjin University, 15(2):79–94. DOI:10.1007/s12209-009-0016-3.

Hager, W.H. (2007) Scour in hydraulic engineering. Water Management 160:159–168. DOI:10.1680/wama.2007.160.3.159.

Hahn, E. M. and Lyn, D. A. (2010) Anomalous Contraction Scour? Vertical-Contraction Case. Journal of Hydraulic Engineering, 136(2):137–141. DOI:10.1061/(asce)0733-9429(2010)136:2(137).

Heller, V. (2011) Scale effects in physical hydraulic engineering models. Journal of Hydraulic Research 49(3):293–306. DOI:10.1080/00221686.2011.578914.

Hirt, C.W., Nichols, B.D. (1981) Volume of fluid (VOF) method for the dynamics of free boundaries. Journal of Copmutational Physics 39(1):201–225. DOI: 10.1016/0021-9991(81)90145-5.

Jiang, G. S. and Peng, D. (2000) Weighted ENO schemes for Hamilton-Jacobi equations. SIAM Journal on Scientific Computing, 21(6): 2126–2143. DOI:10.1137/S106482759732455X.

Johnson, P.A., Ayyub, B.M. (1992) Assessing time-variant bridge reliability due to pier scour. Journal of Hydraulic Engineering, 118(6):887–903. DOI:10.1061/%28ASCE%290733-9429%281992%29118%3A6%28887%29.

Jones, J.S., Bertoldi, D.A., Umbrell, E.R. (1993) Preliminary studies on pressure-flow scour. In: ASCE Conference on Hydruaulic Engineering, ASCE, Reston, VA, USA.

Kamath, A., Fleit, G., Bihs, H. (2019) Investigation of Free Surface Turbulence Damping in RANS Simulations for Complex Free Surface Flows. Water 11(3):456, 26p. DOI:10.3390/w11030456.

Kara, S., Kara, M.C., Stoesser, T., Sturm, T.W. (2015a) Free-Surface versus Rigid-Lid LES Computations for Bridge-Abutment Flow. Journal of Hydraulic Engineering 141(9):04015019, 9p. DOI:10.1061/(asce)hy.1943-7900.0001028.

Kara, S., Stoesser, T., Sturm, T. W. and Mulahasan, S. (2015b) Flow dynamics through a submerged bridge opening with overtopping. Journal of Hydraulic Research, 53(2):186–195. DOI:10.1080/00221686.2014.967821.

Kim, S.S., Nabi, M., Kimura, I., Shimizu, Y. (2014) Numerical investigation of local scour at two adjacent cylinders. Advances in Water Resources 70:131–147. DOI:10.1016/j.advwatres.2014.04.018.

Khosronejad, A., Kang, S., Sotiropoulos, F. (2012) Experimental and computational investigation of local scour around bridge piers. Advances in Water Resources 37:73–85. DOI:10.1016/j.advwatres.2011.09.013.

Khosronejad, A., Flora, K., Kang, S. (2020) Effect of inlet turbulent boundary conditions on scour predictions of coupled LES and morphodynamics in a field-scale river: Bankfull flow conditions. Journal of Hydraulic Engineering 146(4):04020020, 24p. DOI:10.1061/(ASCE)HY.1943-7900.0001719.

Kumcu, S. Y. (2016) Steady and unsteady pressure scour under bridges at clear-water conditions. Canadian Journal of Civil Engineering, 43(4):334–342. DOI:10.1139/cjce-2015-0385.

Kundzewicz, Z.W., Kanae, S., Seneviratne, S.I. et al. (2013) Flood risk and climate change: global and regional perspectives. Hydrological Sciences Journal, 59(1):1–28. DOI:10.1080/02626667.2013.857411.

Lee, D., Nakagawa, H., Kawaike, K., Baba, Y., Zhang, H. (2010) Inundation flow considering overflow due to water level rise by river structures. Annuals of Disas. Prev. Res. Inst., Kyoto University, No. 53 B., 607–616.

Liang, D., Cheng, L., Li, F. (2005) Numerical modeling of flow and scour below a pipeline in currents Part II. Scour simulation. Coastal engineering 52:43–62. DOI:10.1016/j.coastaleng.2004.09.001.

Liang, D., Huang, J., Zhang, J., Shi, S., Zhu, N., Chen, J. (2022) Three-dimensional simulations of scour around pipelines of finite lengths. Journal of Marine Science and Engineering 10:106. DOI:10.3390/jmse10010106.

Liu X-D., Osher, S., Chan, T. (1994) Weighted Essentially Non-oscillatory Schemes. Journal of Computational Physics 115(1):200–212. DOI:10.1006/jcph.1994.1187.

Martín-Vide, J. P. and Prió, J. M. (2005) Backwater of arch bridges under free and submerged conditions. Journal of Hydraulic Research, 43(5):515–521. DOI:10.1080/00221680509500149.

Malavasi, S., Guadagnini, A. (2003) Hydrodynamic Loading on River Bridges. Journal of Hydraulic Engineering 129(11):854–861. DOI:10.1061/(ASCE)0733-9429(2003)129:11(854).

Malavasi, S., Guadagnini, A. (2007) Interactions between a rectangular cylinder and a free-surface flow. Journal of Fluids and Structures 23(8):1137–1148. DOI:10.1016/j.jfluidstructs.2007.04.002.

Nguyen, V.T., Nestmann, F. (2004) Applications of CFD in Hydraulics and River Engineering. International Journal of Computational Fluid Dynamics 18(2):165–174. DOI:10.1080/10618560310001634186.

Olsen, N. R. B. and Melaaen, M. C. (1993) Three-Dimensional Calculation of Scour Around Cylinders. Journal of Hydraulic Engineering, 119(9):1048–1054. DOI:10.1061/(asce)0733-9429(1993)119:9(1048).

Paola, C. and Voller, V. R. (2005) A generalized Exner equation for sediment mass balance. Journal of Geophysical Research: Earth Surface, 110(4):F04014, 8p. DOI:10.1029/2004JF000274.

Rodi, W. (1980) Turbulence models and Their Application in Hydraulics – A State of the Art Review. International Association for Hydraulics Research, Delft, the Netherlands.

Roulund, A., Sumer, B. M., Fredsøe, J. and Michelsen, J. (2005) Numerical and experimental investigation of flow and scour around a circular pile. Journal of Fluid Mechanics, 534:351–401. DOI:10.1017/S0022112005004507.

Shen, J., Shan, H., Suaznabar, O., Xie, Z., Lottes, S. and Kerenyi, K. (2012) Submerged-flow bridge scour under clear-water conditions. In ICSE6, 27-31 August, 2012, Paris, France, pp. 755–760.

Szydłowski, M. (2011) Numerical Simulation of Open Channel Flow between Bridge Piers. TASK QUARTERLY 15(3):271–282.

Tulimilli, B. R., Lottes, S. A., Majumdar, P. and Kostic, M. (2011) Three-dimensional scouring analysis for open channel pressure flow scour under flooded bridge decks. ASME 2011 International Mechanical Engineering Congress and Exposition, IMECE 2011, 6(PARTS A AND B), 975–981. DOI:10.1115/imece2011-65529.

Umbrell, E. R., Young, G. K., Stein, S. M. and Jones, J. S. (1998) Clear-water contraction scour under bridges in pressure flow. Journal of Hydraulic Engineering, 124(2):236–240. DOI:10.1061/(ASCE)0733-9429(1998)124:2(236).

van Rijn, L. C. (1984) Sediment transport, part I: Bed load transport. Journal of Hydraulic Engineering, 110(10):1431–1456. DOI:10.1061/(ASCE)0733-9429(1984)110:10(1431).

Wilcox, D.C. (1994) Turbulence Modeling for CFD; DCW Industries Inc.: La Canada, CA, USA, 1994.

Xie, Z. (2011) Theoretical and numerical research on sediment transport in pressurized flow conditions. Civil Engineering Theses, Dissertations and Student Research. Paper 23., 217p. University of Nebraska – Lincoln, US. Link: https://digitalcommons.unl.edu/cgi/viewcontent.cgi?article=1022&context=civilengdiss.